1995ApJ...449..576R

THE ASTROPHYSICAL JOURNAL, 449:576–591, 1995 August 20

DUST AND MOLECULAR GAS IN THE BARRED SPIRAL GALAXY NGC 1530

MICHAEL W. REGAN,[1,2] STUART N. VOGEL,[3] AND PETER J. TEUBEN[4]
Department of Astronomy, University of Maryland, College Park, MD 20742

Received 1994 December 20; accepted 1995 March 7

ABSTRACT

We present Berkeley-Illinois-Maryland Array CO ($J = 1$–0) interferometry at 3″ resolution, NRAO 12 m single-dish observations, and KPNO near-infrared observations of the strongly barred spiral galaxy NGC 1530. The CO observations reveal that the molecular gas in the central regions is concentrated near the intersection of the dust lanes and a nuclear dust ring. However, the CO morphology is more complex than a simple "twin peaks" morphology reported for some other barred spirals and is better approximated by a partial ring or partial two-armed spiral.

We combine the near-infrared observations with optical observations of the galaxy to form optical-infrared color maps. These maps reveal an inner dust ring not visible using optical colors alone. We use a radiative transfer model that accounts for both absorption and multiple scattering to model the expected colors for a given amount of dust and a given vertical scale height of the dust relative to the stars. We then use this model to derive the optical depth and relative scale height of the dust throughout the bar and nuclear dust ring of NGC 1530. The peak face-on optical depth we derive is approximately $\tau_V = 4$.

We also show that the ratio of the dust optical depth to the CO emission varies between the bar dust lanes and the nuclear dust ring by a factor of 2. CO emission is relatively enhanced in the nuclear dust ring, which we attribute to heating of the molecular gas by the ongoing star formation in the nuclear region.

Subject headings: dust, extinction — galaxies: individual (NGC 1530) — galaxies: ISM — galaxies: spiral — infrared: galaxies — radio lines: galaxies

1. INTRODUCTION

Understanding barred spirals is critical since one-third of all bright spirals show a bar in the optical (Sandage & Tamman 1981), and near-infrared observations reveal even more galaxies to be barred (Thronson et al. 1989; Block et al. 1994). Bars have also been postulated as driving gas into the center of galaxies, fueling active galactic nuclei (AGNs) and starbursts. Models show that gas will be driven inward when it loses angular momentum after being shocked in the dust lanes along the leading edge of the bar (Athanassoula 1992; Piner, Stone, & Teuben 1993). Both models (Sanders & Tubbs 1980; Athanassoula 1992) and observations (Ondrechen & van der Hulst 1983; Pence & Blackman 1984; Ondrechen 1985; Lindblad & Jörsäter 1987) show that the dust lanes in barred galaxies are the location of shocks. Thus, the morphology of the dust and dense gas can reveal characteristics of the kinematics of the galaxy. The goal of this paper is to understand the characteristics of the dust and gas in the dust lanes and near the center of a barred spiral galaxy.

Low-resolution (FWHM > 7″) millimeter observations of barred spirals reveal that emission from the CO molecule is centrally concentrated (Lo et al. 1984; Sandqvist, Elfhag, & Jörsäter 1988; Handa et al. 1990; Devereux, Kenney, & Young 1992). Existing higher resolution interferometric observations indicate that this central concentration is of two types. Either the emission is concentrated in two peaks where the dust lanes end near the nucleus ("twin peaks"), or it is centered on the nucleus (Kenney et al. 1992; Kenney, Carlstrom, & Young 1993). Kenney et al. (1992) proposed that twin peaks occurred in galaxies with an inner Lindblad resonance (ILR) because the inward flowing gas piles up at the ILR, while in galaxies without an ILR the gas was unimpeded as it flowed into the nucleus, leading to a central concentration.

Many barred spiral galaxies show nuclear rings of young stars when observed through blue or visual filters (Buta 1986). These nuclear rings are thought to be the sites of active star formation brought about by the bar-driven inflow of gas to the ILR. Buta & Crocker (1993) summarize the characteristics of the nuclear rings in a sample of spiral galaxies. They find that there is a strong correlation between the presence of a nuclear ring and straight dust lanes in the bar of the galaxy. Athanassoula (1992) discussed how straight dust lanes in the bar only form when the galaxy has an ILR. Thus, nuclear rings are probably related to an ILR (Buta & Crocker 1993).

This paper is the first in a series to study the strongly barred spiral galaxy NGC 1530. The global characteristics of NGC 1530 are summarized in Table 1. Using a value of $H_0 = 75$ and $V_{\rm LG} = 2600$ km s^{-1} for NGC 1530 (Young et al. 1989), we adopt a distance of 35 Mpc to NGC 1530. At this assumed distance the deprojected bar is one of the largest known (29 kpc). A nuclear blue star-forming ring has been observed in NGC 1530 (Buta & Crocker 1993) with a radius of 23″ (4 kpc). The large apparent size of the bar in NGC 1530 compensates for the large distance to the galaxy, allowing for the structure of the bar to be well studied. In this paper we will discuss near-infrared and CO observations of NGC 1530. In a future paper (Regan et al. 1995, hereafter Paper II) we will discuss the Hα and H I kinematics and the optical observations.

---

[1] Visiting Astronomer, Kitt Peak National Observatory, National Optical Astronomy Observatories, operated by the Association of Universities for Research in Astronomy, Inc., under contract with the National Science Foundation.

[2] mregan@astro.umd.edu.

[3] vogel@astro.umd.edu.

[4] teuben@astro.umd.edu.

TABLE 1

Global Properties of NGC 1530

Parameter	Value	Reference
K-band Peak:		
R.A. (J2000)	$4^{h}23^{m}26^{s}.7$	1
decl. (J2000)	75°17′43″.8	1
Optical size (D_{25})	4′.9	2
Inclination	55°	3
Systematic radial velocity (LSR)	2457 ± 3 km s^{-1}	3
Adopted distance	35 Mpc	...
Linear scale	165 pc arcsec^{-1}	...
Bar length	100″	1
Bar position angle	121°	1
Nuclear ring radius	21″	4
H I line width at 20% of peak	346 km s^{-1}	3
60 μm flux density	10.3 (Jy)	2
100 μm flux density	24.4 (Jy)	2
Dust temperature	33.8	2
H I flux	34.4 (Jy km s^{-1})	2
CO (1–0) flux	450 (Jy km s^{-1})	2

References.—(1) This paper; (2) Young et al. 1989; (3) Staveley-Smith & Davies 1987; (4) Buta & Crocker 1993.

2. OBSERVATIONS AND DATA REDUCTION

2.1. *COB and SQIID Infrared Array Observations*

Observations were obtained in the near-infrared *J* and *K′* bands (Wainscoat & Cowie 1992) using the Cryogenic Optical Bench (COB) on the 1.3 m telescope at Kitt Peak on the nights of 1994 March 4, 7, 9, and 10. COB uses a 256 × 256 InSb detector and has 0″.95 pixels on the 1.3 m telescope yielding a 4′ field of view. Owing to undersampling of the seeing, the effective resolution was 1″.7 FWHM. In *K′* we used 20 s exposures that were co-added 6 times before reading for a total exposure time of 120 s. In *J* we used 40 s exposures that were co-added 3 times before reading for a total exposure time of 120 s. After a pair of dithered objects exposures were taken, the telescope was slewed 15′ south or north, and a pair of dithered sky exposures were taken. The total exposure times were 36 minutes and 38 minutes in *J* and *K′*, respectively.

The data reduction process was similar to that described in Regan & Vogel (1994). The flat field in *J* varied when switching between J band and *K′* band, so separate flat fields for each set of *J*-band frames were formed by median-filtering all the dark subtracted *J*-band sky exposures taken between changing filters. The flat field in *K′* was constant, so we formed a flat field for each night using all the sky exposures obtained that night. A separate sky frame was formed for each pair of object exposures by median-filtering the four sky exposures taken before and after the object pair. We then subtracted the sky frame, flat-fielded, flipped to the correct north-south orientation, and corrected for extinction. The frames were then registered with each other using stars in the regions of overlap. The final mosaic in each band was created by using the χ^2 minimization technique of Regan & Gruendl (1995). This technique uses all the information in the regions of overlap to find the best background offset for each frame. We were able to obtain the correct zero point for each image from a series of overlapping exposures that extended far enough from the galaxy (8′) to obtain the true sky level.

Other near-infrared observations were also obtained in *J*, *H*, and *K* bands using the Simultaneous Quad Infrared Imaging Device (SQIID) on the 1.3 m telescope at Kitt Peak on the nights of 1994 January 16, 17, and 18. We used 3 minute exposures and again alternated pairs of sky and object exposures. The total exposure time was 81 minutes in *H* band. We only report on the SQIID *H*-band observations here because the COB observations at *J* and *K′* have a much higher signal-to-noise ratio. We used the same methods to reduce the SQIID and COB data.

We performed astrometry on the near-infrared images using the locations of stars from the Hubble Guide Star Catalog. The astrometric solutions are good to about 1″. Infrared standards (Elias et al. 1982; Casali & Hawarden 1992) were observed to calibrate the infrared images and to derive the extinction coefficients.

2.2. *BIMA* CO *1–0 Interferometric and NRAO 12 Meter Single-Dish Observations*

Berkeley-Illinois-Maryland Array (BIMA) observations of the CO $J = 1$–0 line toward NGC 1530 were made in three configurations of six 6.1 m antennas between 1993 November and 1994 January. During this time interval, the antennas were equipped with one SIS and five Schottky receivers, and the single-sideband system temperatures ranged from 500–2000 K, with the average being around 900 K. The digital correlator was configured to provide 4.0 km s^{-1} velocity resolution. Two of the correlator windows were positioned to overlap the other windows so that the total velocity coverage was from 2200 to 2720 km s^{-1}. Projected baselines ranged from 1.5 to 90 kλ. The instrumental gain and phase were calibrated from observations of the quasars 0217 + 738 and 0841 + 708 every 30 minutes, and structure in the IF passband was calibrated with observations of a strong quasar (3C 454.3 or 3C 84). The flux density scale was established by using observations of the quasar 3C 454.3, whose flux was determined by observations of Uranus to range from 12.0 Jy to 14.7 Jy during the period of the observations. We estimate the uncertainty in the flux calibrations to be 30%.

We created a naturally weighted map of the CO data with 8 km s^{-1} channels and cleaned the map using the Högbom algorithm. We then performed an iterative phase-only self-calibration process (Thompson, Moran, & Swensen 1986). For each solution interval of 30 minutes, the phases for each baseline calculated from bright clean components were compared with the measured phases for each channel and used to derive a single, channel-independent phase correction for each antenna. Using multiple channels offers a better signal-to-noise ratio in the gain solution than would a single channel. Averaging the channels prior to the self-calibration procedure would be less optimal because emission structure would tend to be more extended, and therefore visibilities would be reduced. We then applied the phase corrections to each antenna and made a new channel map of the galaxy. The mapping self-calibration process was repeated 3 times, after which the phase corrections were not changing between iterations. This self-calibration increased the peak signal by 30%. No correction for primary beam attenuation was made. Owing to the variation in the noise on the different baselines, the visibilities were weighted by the inverse of the theoretical variance for each baseline. The theoretical variance was determined based on the system temperature of each baseline.

In order to obtain the visibilities shorter than a dish diameter, we observed NGC 1530 at the NRAO[5] 12 m telescope in

---

[5] The National Radio Astronomy Observatory is operated by Associated Universities, Inc., under cooperative agreement with the National Science Foundation.

1995ApJ...449..576R

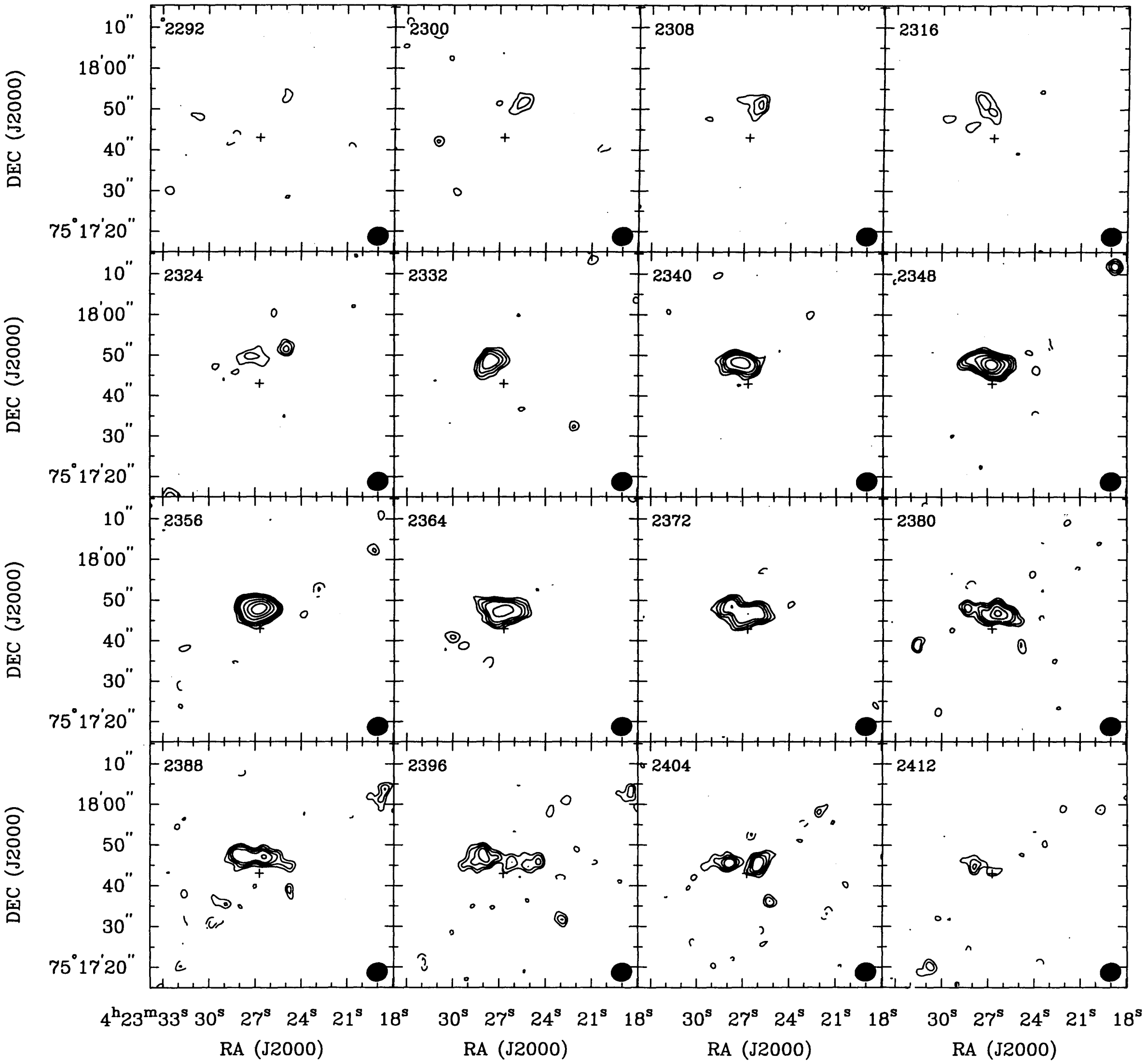

FIG. 1.—Naturally weighted channel maps of the CO 1–0 emission from NGC 1530. The channels have a width of 8 km s^{-1}, and the noise in the individual channels is 0.050 Jy beam^{-1}. The contours are at -3, 3, 4, 5, 6, 8, 10, and 12 σ. The cross in each channel is the K'-band peak of NGC 1530. The synthesized beam is shown in the bottom right of each panel. The central velocity ($V_{\rm lsr}$) is indicated in the upper left of each panel.

1994 October. A total of 22 positions at 30" spacing were obtained to map the galaxy out to a radius of 1'. Two to four 6 minute scans were obtained at each position. The 256 channel 2 MHz (5.2 km s^{-1}) filter bank was configured in parallel mode to detect both polarizations. The data were fitted with linear baselines, and the two polarizations were averaged together. The single-dish spectra were combined with the interferometer observations using the method of Vogel et al. (1984).

The naturally weighted channel maps including the interferometer and single-dish data (Fig. 1) have the best sensitivity to extended structure and result in a 5".2 by 4".5 beam with a position angle of $-74°$; the rms noise level is 0.05 Jy beam^{-1} in the 8 km s^{-1} interval. We created a total intensity map (Fig. 2) from the channel maps by summing all the flux with $|S_v| >$ 0.10 Jy beam^{-1} (2 σ) to minimize the contribution of the noise.

To better reveal the small-scale structure we also made a higher resolution map using uniform weighting with the Fourier transform of a 2" FWHM Gaussian taper applied to the visibilities. This results in a 3".6 by 3".0 beam with a position angle of $-71°.5$ and a rms noise level of 0.09 Jy beam^{-1} in the 8 km s^{-1} channels. We created a high-resolution total intensity map (Fig. 3) by summing all the flux with $|S_v| > 0.18$ Jy beam^{-1} (2 σ).

3. RESULTS

3.1. *Broadband Images and Colors*

Figure 4 shows the near-infrared images of NGC 1530. The central bar has a length of 100" or 17 kpc in the plane of the sky at our assumed distance of 35 Mpc. This leads to a deprojected length of 29 kpc. An asymmetry in the bar centroid relative to the central bulge is most apparent in the J-band image (Fig. 4, *top*) with the eastern half being offset to the south and the western half being offset to the north. Close inspection also shows that the bulge isophotes in the J-band image are not elliptical but show indentations in the northeast and

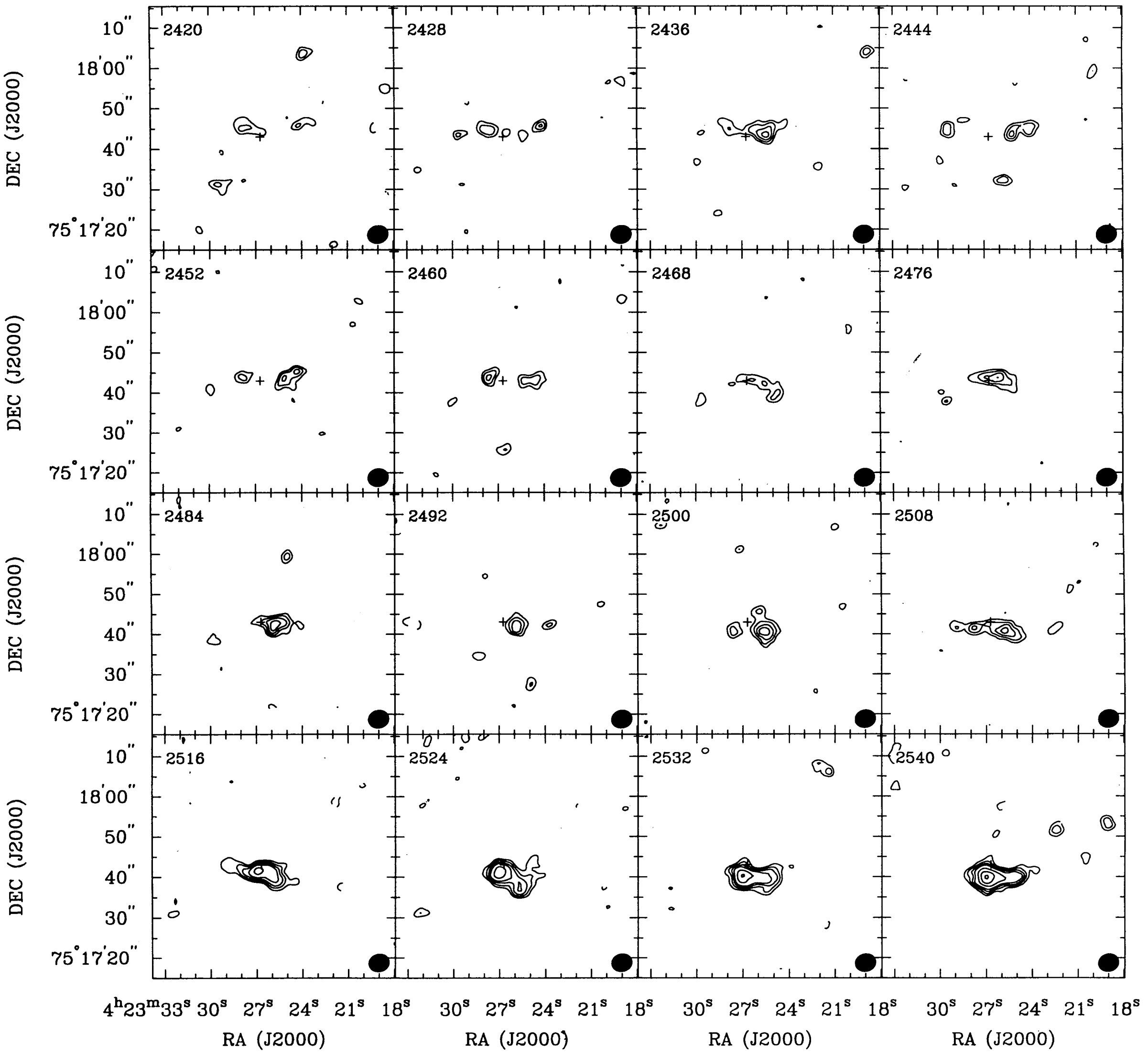

FIG. 1—*Continued*

southwest. These effects are also present in the other bands but become less pronounced at the longer wavelengths, implying that dust extinction may be distorting the isophotes.

To bring out the dust features, the optical images of Paper II and the J- and H-band images were divided into the K'-band image. Although these ratio maps are not formally color maps, they will be referred to as color maps in this paper. The resulting color maps are shown in Figure 5. The $H-K$ map is not shown due to the poor signal-to-noise ratio of the H-band image. In the $B-K'$ and $V-K'$ images, the dust lanes along the leading edge of the bar are quite prominent, but the reddest colors are in the central region. The red colors are caused by extinction rather than excess K-band emission since the K-band morphology shows a deficit of emission at the locations of the reddest colors. This is the opposite of what would be observed if the red colors were caused by excess K-band emission. The importance of using the optical–near-infrared colors to look for dust extinction can be seen by comparing the $B-R$ colors (Fig 5, *bottom right*) to the $B-K'$ colors (Fig. 5, *top left*). Note that in the $B-R$ image none of the central extinction is visible, and the colors are actually dominated by blue excesses to the northwest and southeast of the bulge. In § 4 we will show how embedded dust can be difficult to detect in optical colors but revealed in optical-infrared colors.

3.2. *CP Morphology*

Figure 1 shows the naturally weighted channel maps in the velocity range $2292 < V_{\rm LSR} < 2620$ km s^{-1}. The maps reveal two main concentrations of gas, one to the northeast of the nucleus at a velocity of ~ 2356 km s^{-1} and one to the southwest at a velocity of ~ 2548 km s^{-1}. The total intensity map (Fig. 2) shows the two concentrations of molecular gas seen in other barred spiral galaxies (Kenney et al. 1992) but also shows that the morphology is more complex than just twin peaks. Both the northern and southern emission peaks are extended inside of where the straight dust lanes begin to curve into the nuclear ring. Both are also extended out along the bar dust lanes, especially the southern peak. We can also see some emission coincident with the bar dust lanes to the northwest and the southeast.

1995ApJ...449..576R

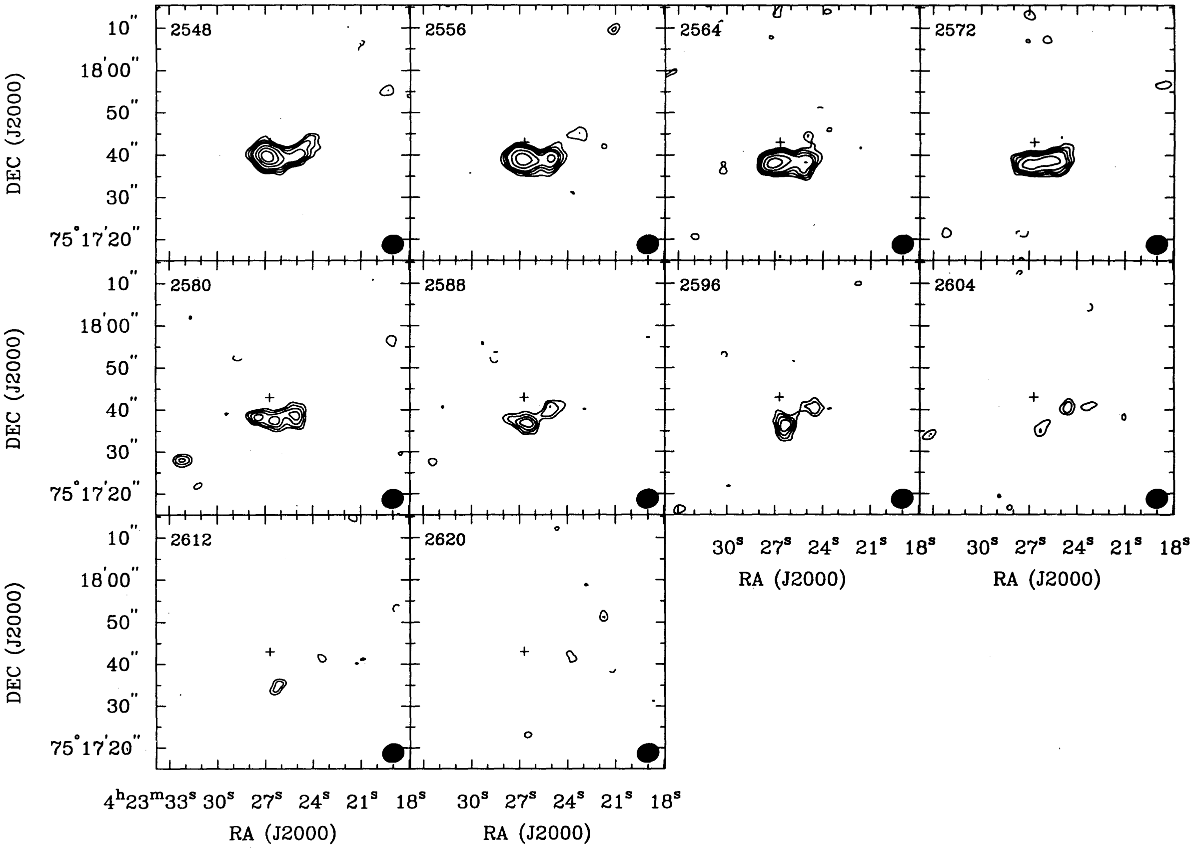

FIG. 1—*Continued*

The higher resolution total intensity map (Fig. 3) shows that the two extended emission regions decompose into several peaks. The overall pattern can be described as a broken ring or a patchy two-armed spiral. If it is a ring, it is not symmetrical about the nucleus. The pattern is only vaguely spiral, with the northern arm curving and the southern arm being rather straight.

3.3. CO *versus Dust Morphology*

We can compare the CO distribution to the reddening by overlaying the CO total intensity map (*contours*) on the $I-K$ color map (*gray scale*) (Fig. 6). In the central regions of NGC 1530 the CO and the $I-K$ colors trace each other quite well, but at the dust lanes in the bar, there is still significant reddening in the $I-K$ colors in regions were the CO is barely detected. In § 4.1 we use the colors as input to a radiative transfer model to determine the optical depth and show that the difference in optical depth does not account for the weakness of CO in the dust lanes.

4. DISCUSSION

4.1. *Dust Optical Depth*

Dust extinction in galaxies cannot be estimated using a simple intervening screen dust model since the dust is embedded within the stellar disk. (Witt, Thronson, & Capuano 1992). Witt et al. (1992) showed that when the dust is embedded in the stellar disk, the observed optical colors of galaxies can be close to the colors that would be observed in the absence of dust extinction. This happens because at reasonable optical depths the dust blocks most of the light from the reddened stars, and the stars on the near side of the dust dominate the emission, leading to unreddened colors. If we use colors that have the K band as the long-wavelength filter and optical bands as the short-wavelength filter, this effect can be avoided over a much higher range of V-band optical depths since the K band has a much lower relative extinction ($A_K = 0.1A_V$). Another advantage of using optical-infrared colors is that a given amount of dust will have a greater effect on an optical-infrared color than it will have on an optical-optical color. For example, if the $B-V$ color excess of an intervening screen of dust is 0.1 mag, the $B-K$ color excess would be 0.4 mag. These two effects explain the differences that are seen between the $B-R$ color map (Fig. 5, *bottom right*) and the $B-K$ color map (Fig. 5, *top left*) of NGC 1530. The straight dust lanes seen in the $B-R$ color map are much stronger in the $B-K$ color map owing to the greater leverage of the optical-infrared color. No reddening due to the nuclear dust ring is seen in the $B-R$ map because the extinction is high enough to block most of the R-band emission from the far side, but the K-band emission is not as severely affected, so a strong reddening is seen in the $B-K$ color.

Another problem with using only optical-optical colors to look for dust extinction is the relatively high albedo of dust grains in the optical. This can cause scattering off dust grains to mask the effects of dust at some optical depths (Witt et al. 1992). If infrared-infrared colors such as $J-K$ are used, then the effect of scattering can be minimized since dust albedos are much lower in the near-infrared. Although there is less leverage on the color excess when using infrared-infrared colors, the

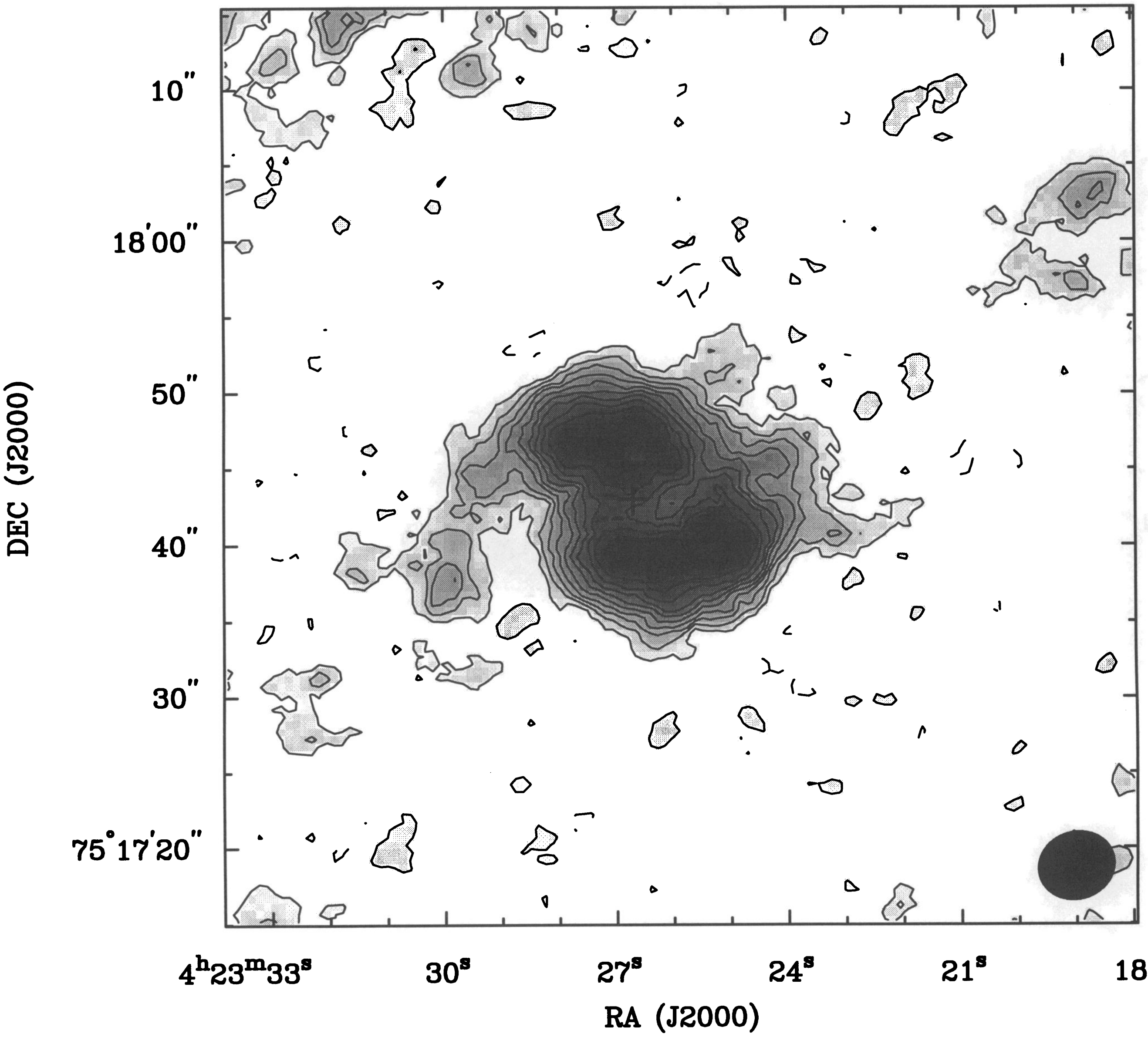

FIG. 2.—Naturally weighted total intensity map of the total CO 1–0 emission from NGC 1530. Only the emission with $|S_v| > 0.10$ Jy beam^{-1} in the individual channels was added into the sum. The contours are at −4, −2, 2, 4, 6, 8, 10, 12, 14, 16, 18, 20, and 22 σ, where σ is 1.60 Jy km s^{-1} beam^{-1}. The cross is the center of the galaxy determined from the K'-band peak. The beam is shown at the bottom right.

color changes due to population variations are much smaller in infrared-infrared colors than in optical-optical or optical-infrared colors, leading to a more reliable estimate of the true change in color due to dust.

To better understand the dust distribution in NGC 1530 we can use the color maps as input to a model of the vertical distribution and optical depth of the dust. We use a model similar to the one Rix & Rieke (1993) used for modeling the dust lanes in M51. Our model differs from their model in that we account for isotropic multiple scattering of the light off dust grains instead of just isotropic single scattering. We use the opacities and albedos from Bruzual, Magris, & Calvet (1988). Like Rix & Rieke (1993) we model the stars and dust with Gaussian vertical distributions centered at the midplane of the disk. There are only two free parameters in the model: ξ, the ratio of the scale height of the dust relative to the scale height of the stars, and τ_V, the face-on total optical depth of the dust in the disk.

This model gives us the ability to probe the three-dimensional structure of the dust distribution by looking at the variation of ξ since the expected colors change quite drastically as ξ varies from 0.0 to 1.0. We used multiple scattering because at optical depths greater than 1.0 the approximation of single scattering breaks down. We assume the dust is smoothly distributed. We also assume that the underlying population of stars is uniform. If the intrinsic colors of the underlying population change, then a basic assumption of the model is wrong, and it will not calculate correct parameters.

The quantities that are needed from each color map are the color excesses of the pixels that have been reddened by dust. This requires knowing the amount the color has been reddened compared to its unreddened value. To determine the color

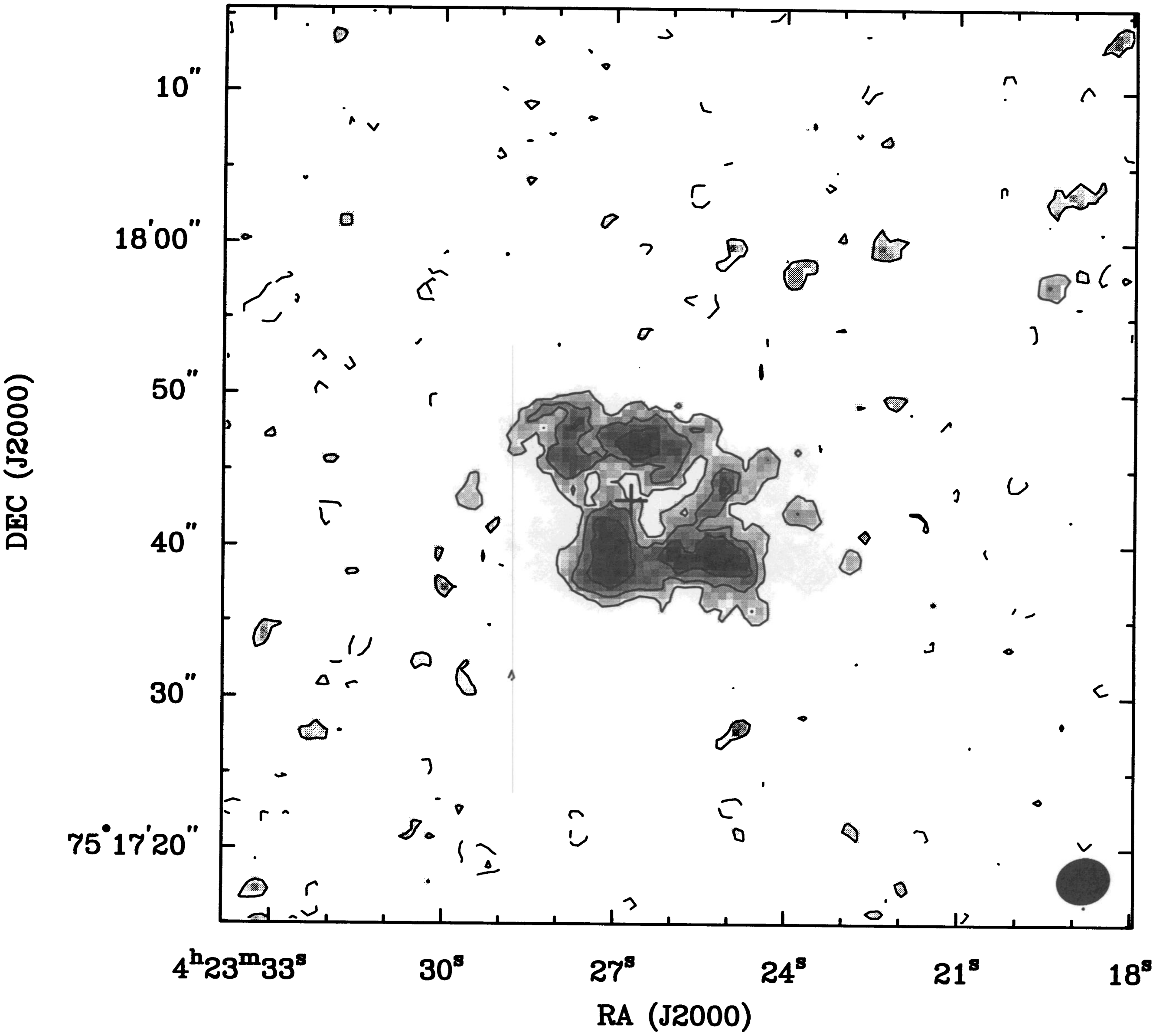

FIG. 3.—Total intensity map of the CO 1–0 emission from NGC 1530 made with uniform weighting and a 2" FWHM Gaussian taper applied to the visibilities. Only the emission with $|S_v| > 0.18$ Jy beam^{-1} in the individual channels was added into the sum. The contours are at -4, -2, 2, 4, 6, and 8 σ, where σ is 2.88 Jy km s^{-1} beam^{-1}. The cross is the center of the galaxy determined from the K'-band peak. The beam is shown at the bottom right.

excess we defined a region in the bar that we determined to be free of extinction by inspection of the $I-K$ map and assumed the color of the region to be the unreddened color. Then, for each color map X, we compared the $X-K$ color in the dust-free region to the $X-K$ color of those pixels that were above a cutoff intensity value in the K-band image. The uncertainty in each color measurement was estimated from the color variations seen in the dust free region. Thus, six color measurements were used to determine τ_v and ξ for each pixel using a χ^2 minimization technique. Since the stellar population of the dust-free region may be different from the stellar population in the regions with dust, we ran the model several different times using different locations as the dust free regions. The results did vary, leading us to estimate the 3 σ uncertainty in the determination of τ_V to be 20% and the uncertainty in ξ to be 40% when χ^2 is less than 4.0.

Figures 7*a*–7*c* show the values of τ_V, ξ, and the reduced χ^2 output from our model. A ring of dust is revealed, and the two dust lanes along the leading edge of the bar are quite clear. The value of ξ is nearly 1.0 in the dust lanes, showing that the stars and dust have similar scale heights, while in the dust ring, ξ has a value between 0.2 and 0.6, indicating that the stars have a scale height 2–5 times that of the dust. The value of χ^2 is high in some regions of the dust lanes, so the variation seen in ξ may not be real. At the southeastern bar end the value of ξ is very small, implying that here most of the dust is confined to the plane of the galaxy. Rix & Rieke (1993) found a value for ξ of around 0.4 in the dust lanes in the spiral arms of M51. Our peak optical depth in the nuclear dust ring is approximately $\tau_V = 4$, about the same as Rix & Rieke (1993) found for the spiral arms of M51.

There are several regions where the χ^2 values are high,

1995ApJ...449..576R

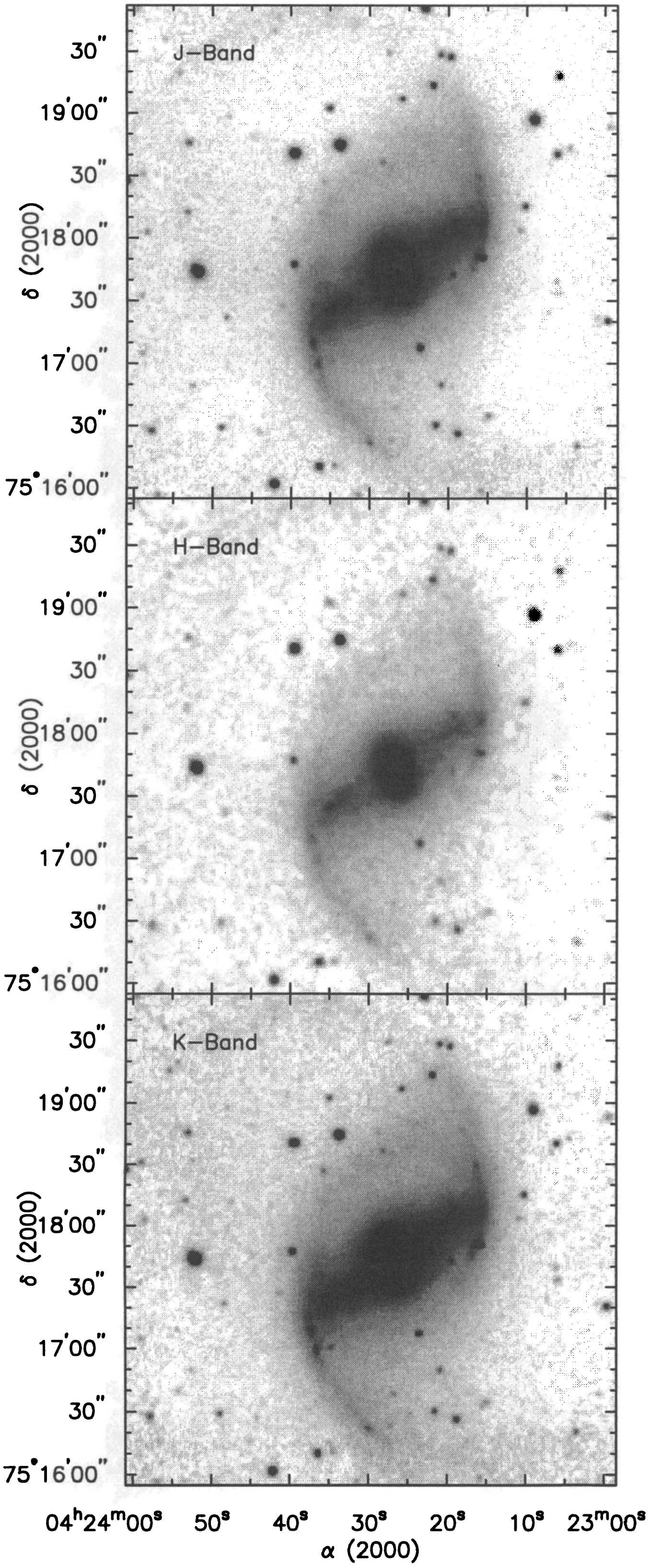

FIG. 4.—Near-infrared images of NGC 1530. (*Top*) *J*-band from COB; (*middle*) *H*-band from SQIID; (*bottom*) *K′*-band from COB.

showing that in a few places the model did not fit the observed colors well. There is a region just north of the nucleus where the χ^2 values are high. The primary cause for this is that the $H-K$ colors in this region are redder than would be expected given the other colors. This occurs at the location of a peak in the CO emission, so it is not clear why the other colors are not as red as the $H-K$ color. The west end of the bar has a region of high χ^2 values. In this region the $V-K$, $B-K$, and $R-K$ colors are blue, while the $I-K$, $J-K$, and $H-K$ colors are red. This is probably a region of active star formation and, thus, the underlying population of stars is not the same as the reference region, leading to incorrect model output. There is a relatively large region in the eastern dust lane where the χ^2 values are high. In this region the problem is that the $B-K$, $V-K$, and $R-K$ colors are too red relative to the $I-K$, $J-K$, and $H-K$ colors. This could be caused by dust above the plane of the stellar disk since our model assumes dust is mixed in with the stars. If so, it would explain why the model determines ξ to be 1.0 in this region since this is the most extended the model can make the dust. Finally, the region outside of the blue emission excess northwest of the nucleus also has high χ^2 values. In this region the $J-K$ and $H-K$ colors show no reddening while the other colors show a low amount of reddening. This could also be due to a small amount of dust above the plane of the galaxy. There are also several localized places where the optical depth determinations are quite high and the χ^2 values are reasonable. In these regions current star formation is causing the model to incorrectly determine the amount of dust. The diversity of reasons for the high χ^2 values shows that this model does not fully reflect the details of the distribution of dust in the galaxy. Even so, it still is very useful for looking at overall patterns in dust distribution.

We measure an angle of 12° between the bar major axis and the straight dust lanes. Assuming that corotation of the bar is just beyond the end of the bar, the angle that the dust lane makes with a bar is a measure of the central concentration of the mass distribution. This is because the dust lane intersects the radius of the ILR at a tangent point, and the ILR moves outward from the center of the galaxy as the mass distribution becomes more centrally concentrated. Thus, the angle between the dust lane and the bar will increase with increasing central mass concentration. Therefore, since the dust lanes in NGC 1530 make a smaller angle with respect to the bar than they do in the Athanassoula standard model (Athanassoula 1992), NGC 1530 has a mass distribution that is less centrally concentrated than her standard model.

Figure 8 shows the naturally weighted CO total intensity map (*contours*) overlaid on the derived optical depth (*gray scale*). Figure 8 implies that the CO optical depth to dust optical depth ratio is not constant since the average values trace each other quite well in the nuclear dust ring but very little to no CO is detected in the dust lanes. Although the dust and CO morphologies agree to first order in the nuclear dust ring, there are differences in their morphologies. For example, the dust ring is complete on the western side of the nucleus over a region where the CO emission becomes weak. This variation in the ratio is discussed further in § 4.3.

4.2. *Ring Structure*

From the CO total intensity maps (Figs. 2 and 3) and the dust extinction map (Fig. 7*a*) it is clear that there is a nuclear ring in the dust and that the molecular gas morphology can be

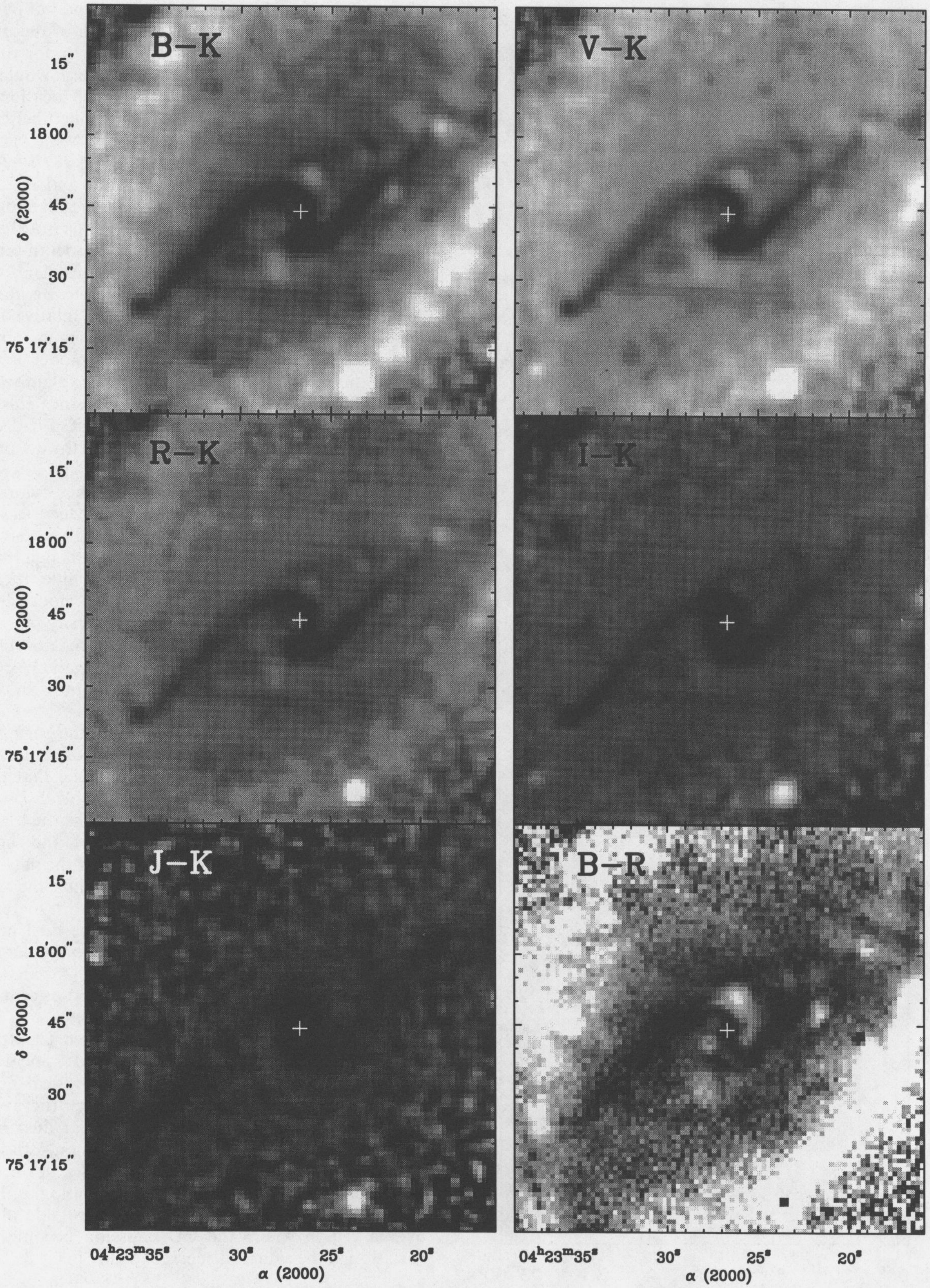

FIG. 5.—Color maps of NGC 1530 formed by dividing each image into the K' map. (*Top left*) $B-K$; (*top right*) $V-K$; (*middle left*) $R-K$; (*middle right*) $I-K$; (*bottom left*) $J-K$; (*bottom right*) $B-R$. The cross is placed at the center of the galaxy as determined from the peak emission in the K-band image. In these maps dark regions are redder colors. Notice that while the dust lanes are visible in the $B-R$ map, the inner region does not show the high level of reddening that is seen in the optical-infrared colors.

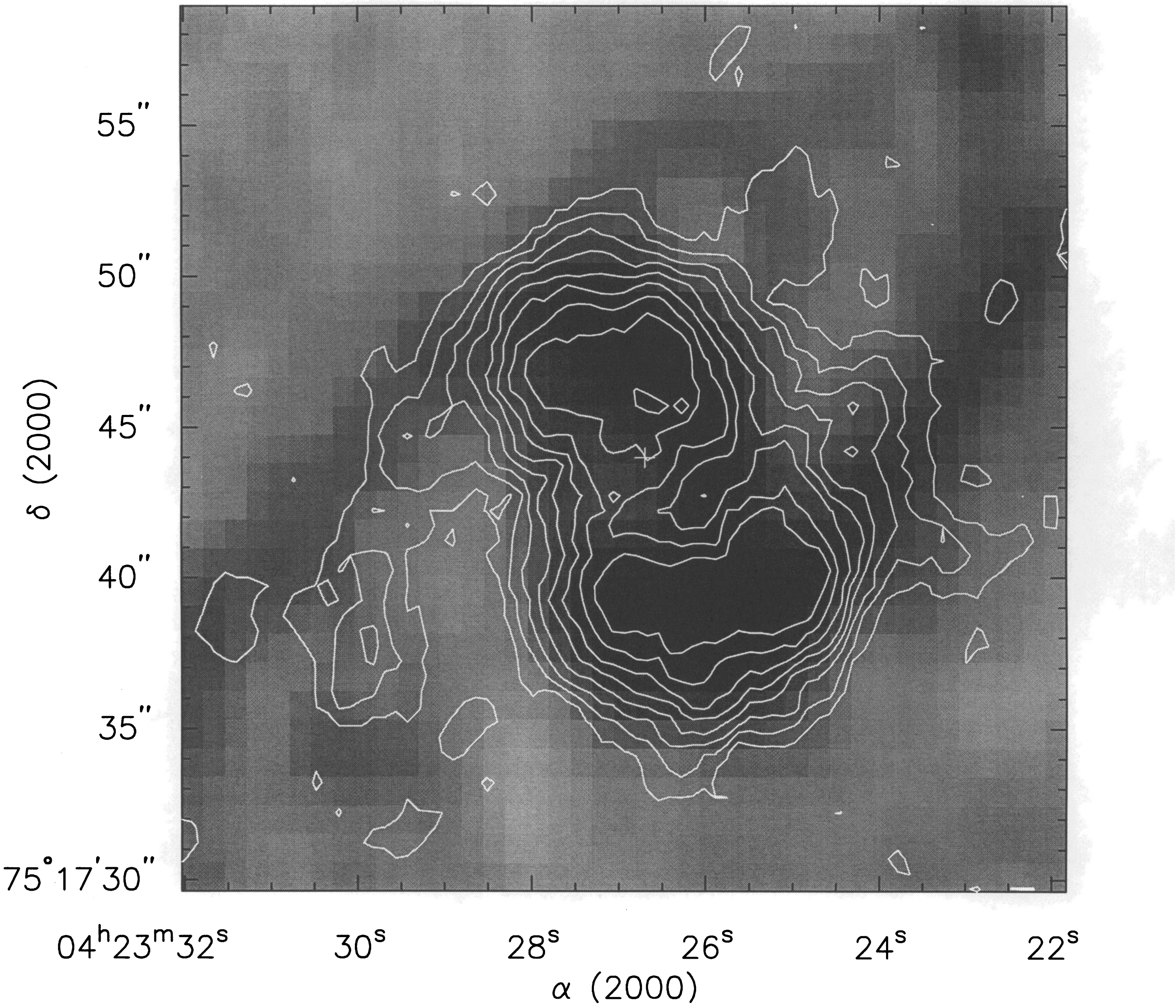

FIG. 6.—CO integrated brightness compared with $I-K$ colors. The contours show the total CO emission (obtained from the total intensity map) seen with the BIMA interferometer. The cross is the center of the galaxy determined from the K'-band peak. The gray scale shows the $I-K$ extinction in NGC 1530. The two track each other well in the inner part of the galaxy, but CO emission is relatively weak in the dust lanes.

approximated by a ring. This ring is nonaxisymmetric in CO, with the highest intensity at the azimuths where it intersects the bar dust lanes and very little emission coming from the azimuths perpendicular to this. These local density peaks in the ring on the opposite sides of the ring would be resolved as just two peaks with a larger beam or poorer coverage in the visibility plane. This suggests that the "twin peaks" seen in other barred spirals are peaks in the density of a ring.

In addition to the dust and gas ring, there is a blue ring that is best seen in the $B-R$ map (Fig. 5, *bottom right*) as the lighter gray-scale colors. This ring is not complete since it is really just a northwest arc and a southeast arc. To first order, the blue arcs have a similar morphology to the CO emission in that they have two main peaks. The ring is truncated at the locations where it crosses the dust lanes. The blue arch to the northwest is directly adjacent to the nuclear dust ring, with the transition from a red color excess to a blue color excess occurring over only 2 pixels (270 pc). The colors of the southeast blue excess do not show a sharp edge but gradually change from a blue excess to a red excess in the dust ring. The blue ring cannot be totally a reflection nebula since no dust shows up at its location in the $J-K$ map where the differential albedo is too small to create blue colors. Some of the blue at the edge of the dust ring is probably caused by reflection off the dust ring since there are locations where the $B-R$ colors are blue while the longer wavelength colors are red.

One scenario that could explain the partial ring morphology of the CO and dust is that the star formation is triggered at the end of the bar dust lanes, and there is a time delay before actual stars form. Once the stars form they continue on their orbits

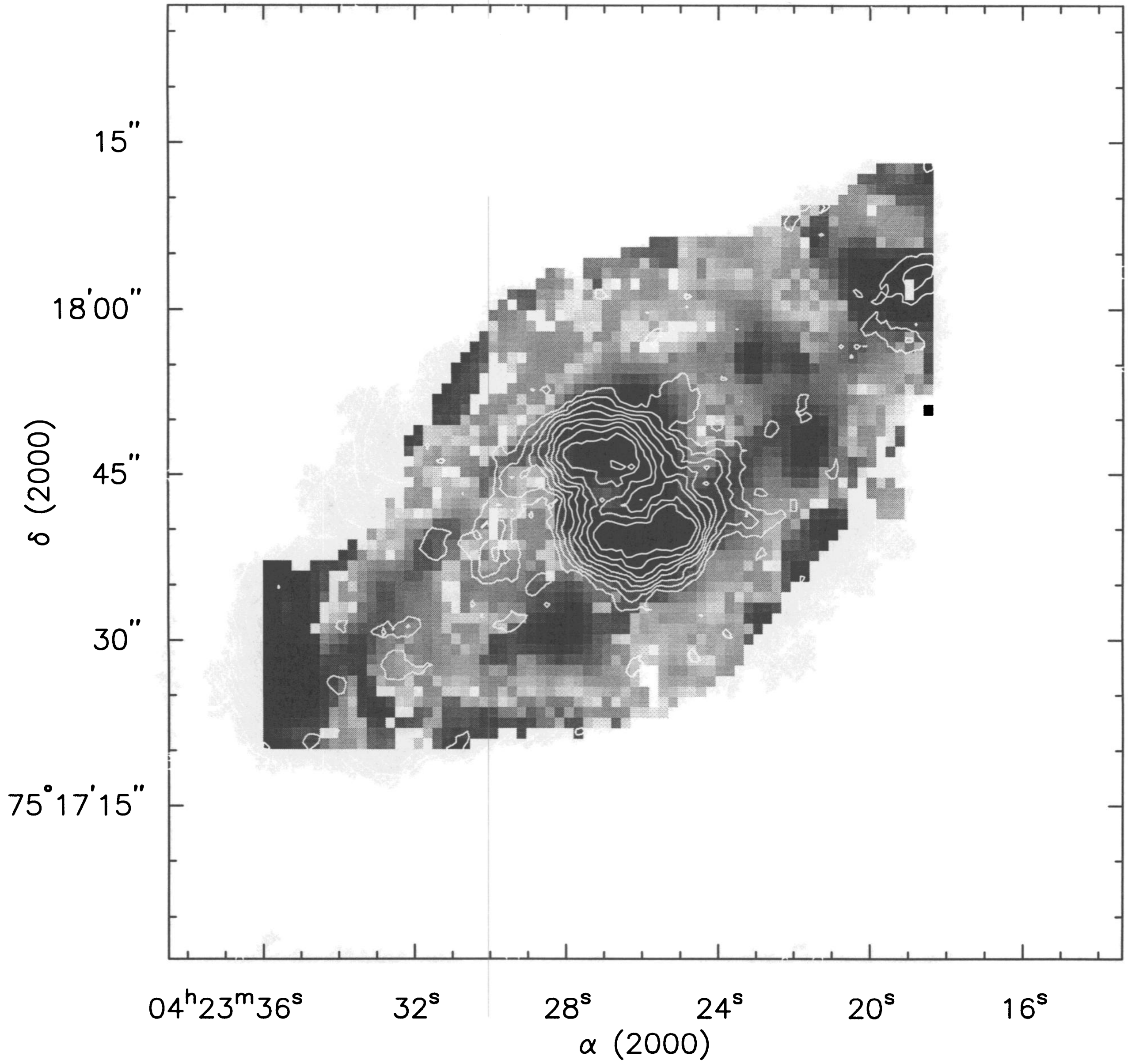

FIG. 7*a*

FIG. 7.—Output from the radiative transfer model that used as input the six $(X-K')$ observed color maps of NGC 1530. (*a*) The face-on total visual optical depth of the dust. The range of the gray scale is from $\tau_V = 0$ to 5. The contours are from 0.5 to 5.0 at intervals of 0.5. (*b*) The ratio of the relative scale height of the dust to the stars. The range in the gray scale is from 0 to 1. The contours are from 0.1 to 1.0 at intervals of 0.1. (*c*) The reduced χ^2 value for each pixel. The range in the gray scale is from 0 to 10. The contours are from 2.0 to 20.0 at intervals of 2.0.

while the gas and dust continue toward the nucleus. One would expect that in this scenario the blue stars would be downstream and at a greater radius than the peak in the dust and molecular gas, as we see in NGC 1530. Another possibility is that the star formation is constant in the blue ring, and the offset seen between the dust peaks and the blue peaks is caused by the high extinction at the innermost extension of the dust lanes. However, if there were significant star formation at the dust peaks it would show up in the *K* band.

The difference in the morphology between the northwest and the southeast blue excesses could be due to the inclination of the galaxy. If the northern side of the galaxy is the near side, then the northwest blue excess would be visible to us without any intervening extinction, while the southeast excess would have to be seen through the vertical extension of the dust from the southern part of the dust ring. This would cause the southeast blue excess to have a more gradual transition into red colors toward the center, while the northern excess would have places where it reflects off the nuclear dust ring. We do see a region inside of the northern excess where the optical colors are blue while the infrared colors are red, implying that reflection is taking place. This shows the importance of including multiple scattering in the model since a single-scattering model cannot replicate the blue optical colors and the red infrared colors. Nonetheless, our model cannot correctly determine the optical depths when the stellar population embedded in the

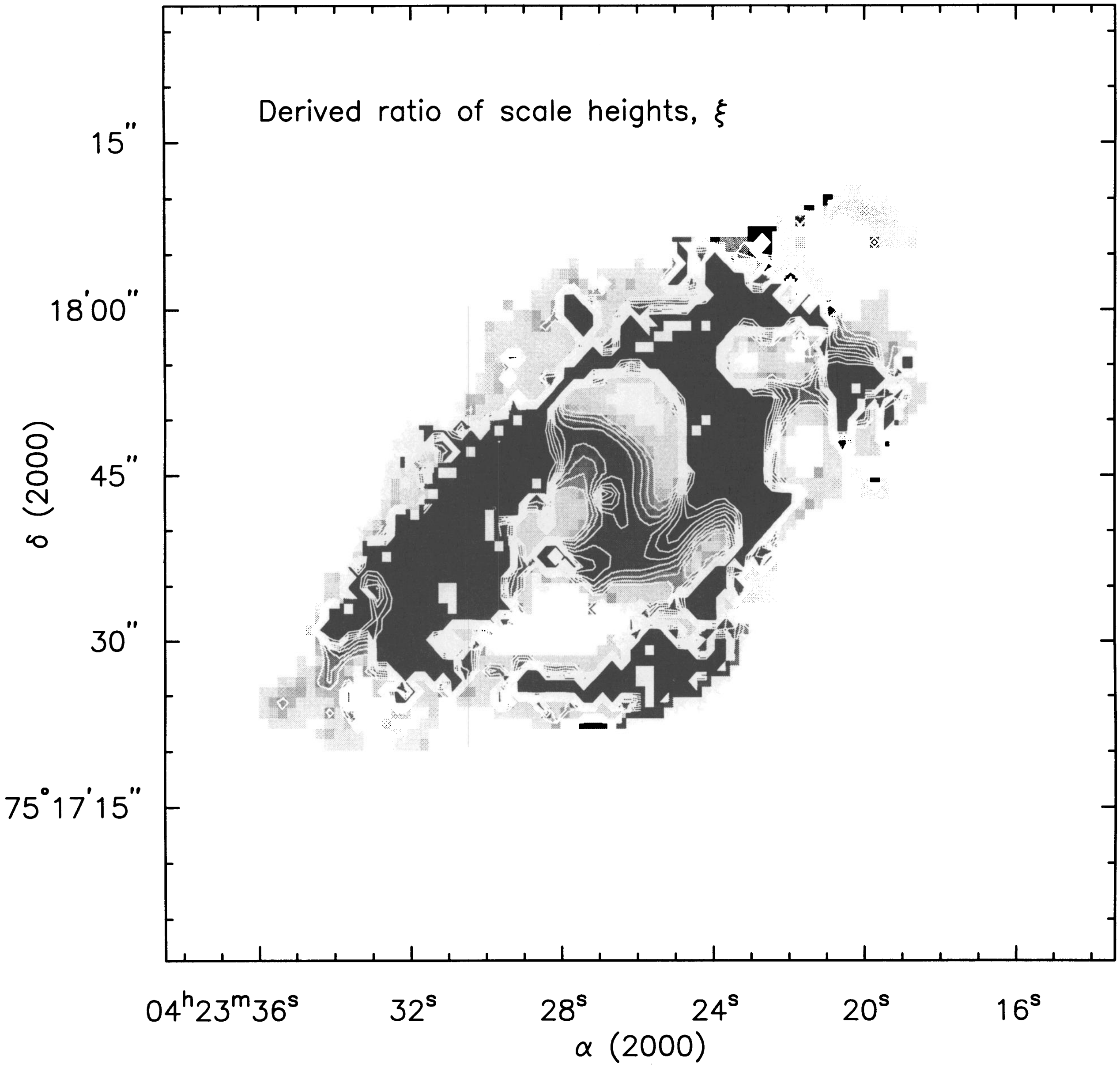

FIG. 7*b*

dust is different than the stellar population in the reference region. Thus, the parameters derived near the edge of the blue excess are uncertain.

4.3. CO/*Dust Ratio Variation*

Figure 8 shows that the CO-to-dust ratio varies between the dust lanes and the nuclear ring. One possible reason for this could be that the interferometer resolved out the relatively extended dust lanes. To test this, we use the map of the dust optical depth and model what the BIMA interferometer would observe if the CO/A_V ratio were constant and using the same coverage in the visibility plane that we have in our BIMA observations. This should be a worst-case test since there is no velocity information in the dust optical depth. This is important since an interferometer will only resolve out a structure that is extended and has a small or zero velocity gradient. Thus, by not using any velocity information in the dust model, we are overestimating the effect of the interferometer resolving out structure. If we compare the output of the modeling (Fig. 9) to the original dust model (Fig 7*a*), we can see that little of the structure is resolved out, and the only difference is the beam smearing due to the 4″ interferometer beam. Thus, the lower ratio of CO emission to dust optical depth in the bar dust lanes is not due to our observing technique.

A typical value of the CO-to-A_V ratio in the nuclear dust ring is 10 Jy km s^{-1} beam^{-1} A_V^{-1}, while in the western dust lane the upper limit is 4 Jy km s^{-1} beam^{-1} A_V^{-1}. Given the star formation that is seen near the nuclear CO emission, it could be that the CO is being heated near the center and thus has a higher CO emissivity relative to the amount of dust. It is also possible that the star formation near the nuclear dust ring has changed the underlying population of stars, causing the model to incorrectly calculate the value of A_V in the dust ring. It is interesting to note that the one region in the western half of the

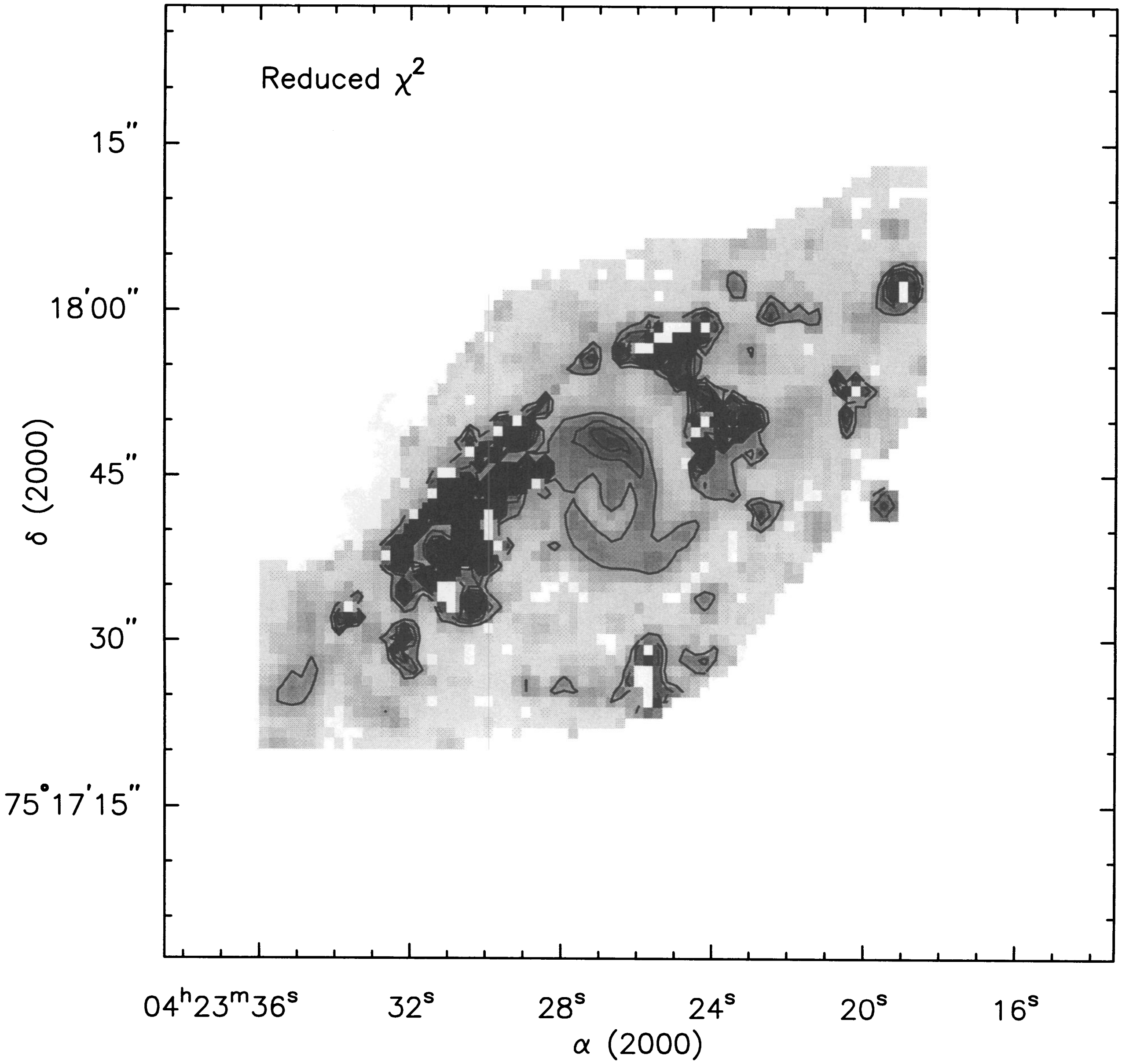

FIG. 7c

bar where we detect CO emission is adjacent to a blue excess visible in the $B-K$ color map (Fig. 5, *top left*). Thus, even here the CO may have been heated by current star formation.

5. CONCLUSIONS

We have shown that the dust extinction in NGC 1530 is clearly revealed by using optical and infrared colors. Our color maps show a nuclear ring of dust extinction that cannot be seen using only optical bands. By using a radiative transfer model that accounts for both absorption and multiple scattering, we are able to derive the face-on optical depth of the dust and the scale height of the dust relative to the stars. The model shows that in the nuclear dust ring the dust scale height is about 0.2–0.6 that of the stars, while at the southeastern bar end the dust is highly confined to the plane of the galaxy. In several regions of the bar dust lanes the model does not reproduce the observed colors well, most likely either because there is dust above the plane of the stellar disk or because there is current star formation in these regions.

Our CO observations of NGC 1530 show that the molecular gas in NGC 1530 is concentrated in the regions where the straight bar dust lanes end at the nuclear dust ring. The CO morphology is more complex than a simple twin peaks since the emission is more extended and looks more like a partial ring or patchy two-armed spiral. One possible explanation of the CO, dust, and star formation morphology is that star formation is triggered at the intersection of the straight bar dust lane, and the ILR and the stars continue on their orbits while the gas not forming stars continues in toward the nucleus.

We also show that there is a variance in the ratio of the dust optical depth to the CO emission between the nuclear ring and the bar dust lanes of at least a factor of 2. The most likely reason for this is heating by recent star formation in the nuclear ring.

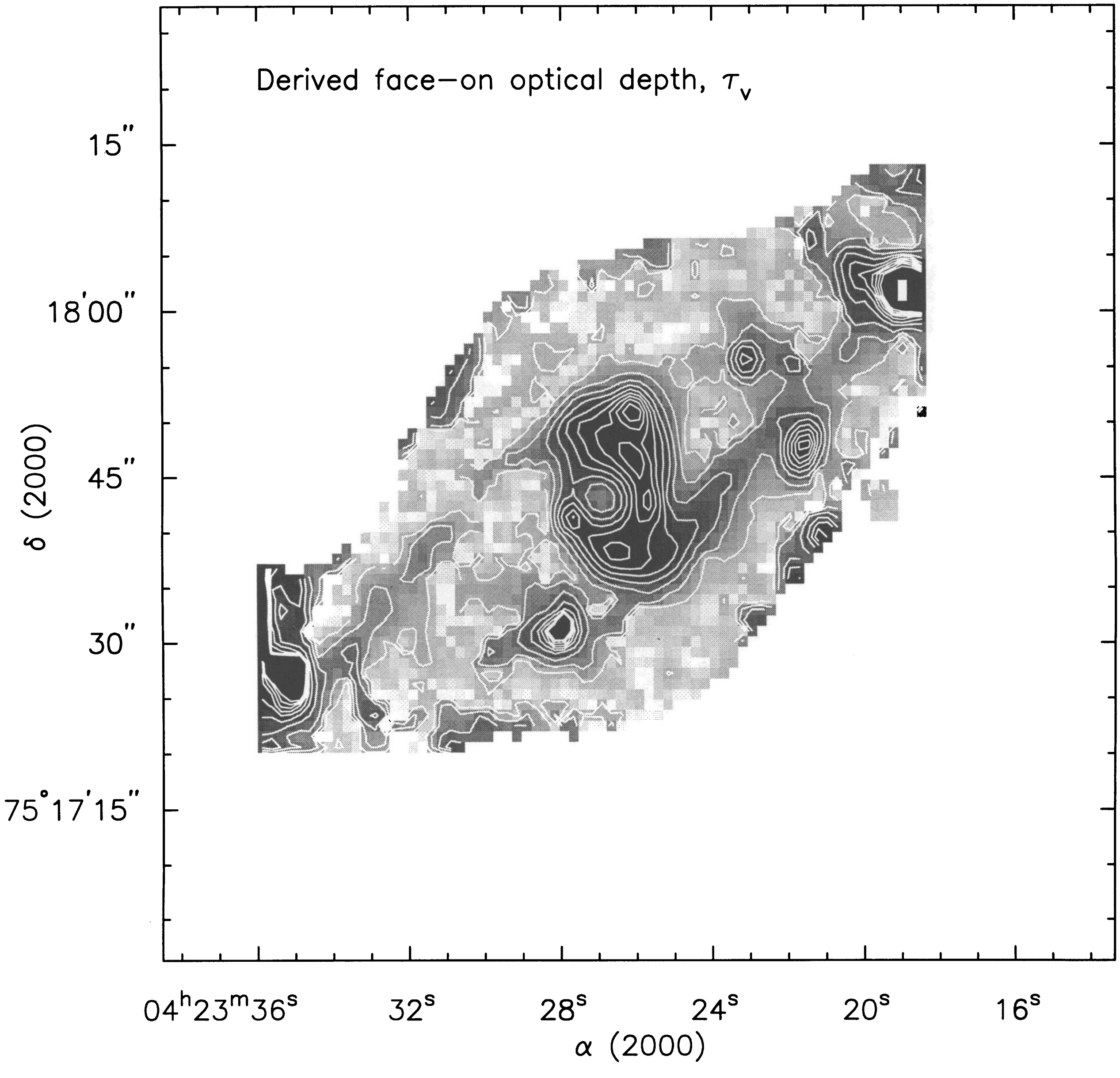

FIG. 8.—CO integrated brightness compared with dust optical depths. The contours show the total CO emission seen with the BIMA interferometer. The gray scale is the model output face-on total optical depth of the dust. The range is from $\tau_V = 0$ to 5. As with the $I-K$ color map, the CO and total dust extinction trace each other well near the nucleus, but the CO is not detected in the bar dust lanes.

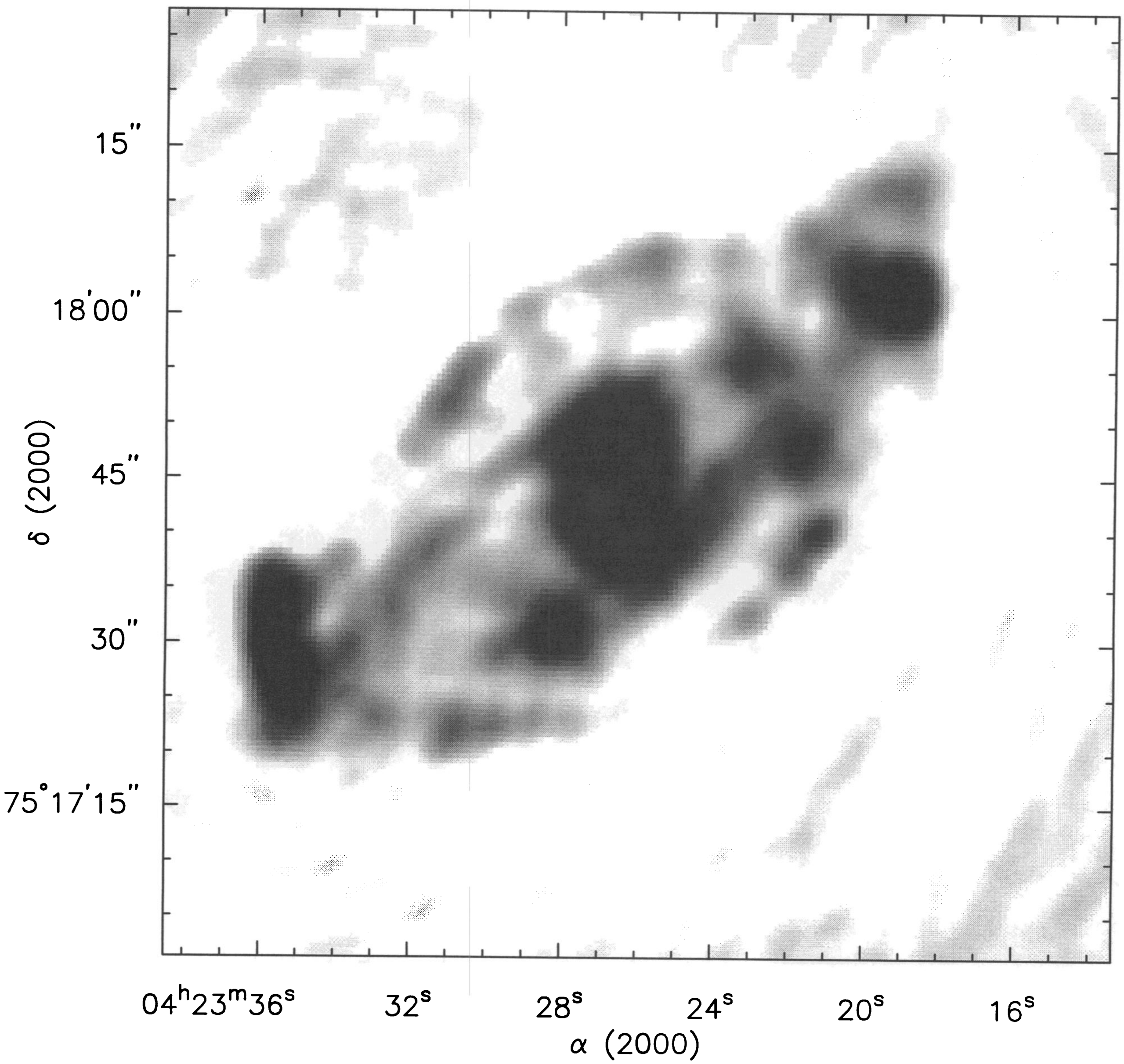

FIG. 9.—What the BIMA interferometer would observe if the CO emission had the morphology of the dust optical depth. Notice that the interferometer would be able to resolve and detect the bar dust lanes. This is a worst-case test since the real observations contain velocity information and therefore resolving out extended structure should be less of a problem.

We would like to thank Michele Thornley for help with both the infrared observations and the single-dish observations, and Robert Gruendl for help with the infrared observations. We would also like to thank the BIMA staff for help with the observations. This work was supported in part by NSF grant AST 93-14847.

REFERENCES

Athanassoula, E. 1992, MNRAS, 259, 345

Block, D. L., Bertin, G., Stockton, A., Grosbøl, P., Moorwood, A. F. M., & Peletier, R. F. 1994, A&A, 288, 365

Buta, R. 1986, ApJS, 61, 609

Buta, R., & Crocker, D. A. 1993, AJ, 105, 1344

Bruzual, A. G., Magris, G., & Calvet, N. 1988, ApJ, 333, 673

Casali, M., & Hawarden, T. 1992, The JCMT-UKIRT Newsletter, 4, 33

Devereux, N. A., Kenney, J. D. P., & Young, J. S. 1992, AJ, 103, 784

Elias, J. H., Frogel, J. A., Matthews, K., & Neugebauer, G. 1982, AJ, 87, 1029

Handa, T., Nakai, N., Sofue, Y., Hayashi, M., & Fujimoto, M. 1990, PASJ, 42, 1

Kenney, J. D. P., Carlstrom, J. E., & Young, J. S. 1993, ApJ, 418, 687

Kenney, J. D. P., Wilson, C. D., Scoville, N. Z., Devereux, N. A., & Young, J. S. 1992, ApJ, 395, L79

Lindbland, P. O., & Jörsäter, S. 1987, in Proc. of the 10th European Regional Astronomy Meeting, Evolution of Galaxies, Vol. 4, ed. J. Palous (Ondřejov: Astron. Inst. of Czechoslovakia Acad. Sci.), 289

Lo, K. Y., et al. 1984, ApJ, 282, L59

Ondrechen, M. P. 1985, AJ, 90, 1474

Ondrechen, M. P., & van der Hulst, J. M. 1983, ApJ, 269, L47

Pence, W. D., & Blackman, C. P. 1984, MNRAS, 207, 9

Piner, B. G., Stone, J. M., & Teuben, P. J. 1993, BAAS, 25, 1411

Regan, M. W., & Gruendl, R. A. 1995, Astronomical Data Analysis and Systems IV, ed. R. A. Shaw, H. E. Payne, & J. J. E. Haynes (ASP Conf. Ser., 77), 335

Regan, M. W., Teuben, P. J., Vogel, S. N., & van der Hulst, T. 1995, in preparation

Regan, M. W., & Vogel, S. N. 1994, ApJ, 434, 536

Rix, H. W., & Rieke, M. J. 1993, ApJ, 418, 123

Sandqvist, A., Elfhag, T., & Jörsäter, S. 1988, A&A, 201, 223

Sandage, A., & Tamman, G. A. 1981, in A Revised Shapley Ames Catalog of Bright Galaxies (Carnegie Inst. of Washington Publ. 635)

Sanders, R. H., & Tubbs, A. D. 1980, ApJ, 235, 803

Staveley-Smith, L., & Davies, R. D. 1987, MNRAS, 224, 953

Thompson, A. R., Moran, J. M., & Swenson, G. W. 1986, Interferometry and Synthesis in Radio Astronomy (New York: Wiley)

Thronson, H. A. J., et al. 1989, ApJ, 343, 158

Vogel, S. N., Wright, M. C. H., Plambeck, R. L., & Welch, W. J. 1984, ApJ, 283, 655

Wainscoat, R. J., & Cowie, L. L. 1992, AJ, 103, 332

Witt, A. D., Thronson, H. A., & Capuano, J. M. 1992, ApJ, 393, 611

Young, J. S., Xie, S., Kenney, J. D. P., & Rice, W. L. 1989, ApJS, 70, 699